Damping Characteristic Analysis and Optimization of Wind-thermal-bundled Power Transmission by LCC-HVDC Systems

Liwen Zheng and Shiying Ma

***Abstract*—With the rapid development of renewable energy, wind-thermal-bundled power transmission by line-commutated converter based high-voltage direct current (LCC-HVDC) systems has been widely developed. The dynamic interaction mechanisms among permanent magnet synchronous generators (PMSGs), synchronous generators (SGs), and LCC-HVDC system become complex. To deal with this issue, a path analysis method (PAM) is proposed to study the dynamic interaction mechanism, and the damping reconstruction is used to analyze the damping characteristic of the system. First, based on the modular modeling, linearized models for the PMSG subsystem, the LCC-HVDC subsystem, and the SG subsystem are established. Second, based on the closed-loop transfer function diagram of the system, the disturbance transfer path and coupling relationship among subsystems are analyzed by the PAM, and the damping characteristic analysis of the SG-dominated oscillation mode is studied based on the damping reconstruction. Compared with the PAM, the small-signal model of the system is obtained and eigenvalue analysis results are presented. Then, the effect of the control parameters on the damping characteristic is analyzed and the conclusions are verified by time-domain simulations. Finally, the penalty functions of the oscillation modes and decay modes are taken as the objective function, and an optimization strategy based on the Monte Carlo method is proposed to solve the parameter optimization problem. Numerical simulation results are presented to validate the effectiveness of the proposed strategy.**

***Index Terms*—Wind-thermal-bundled power transmission, line-commutated converter based high-voltage direct current (LCC-HVDC), path analysis method (PAM), damping characteristic analysis, Monte Carlo method.**

I. Introduction

With the development of clean energy, the installed capacity of wind power has been gradually increasing. On the one hand, large-scale wind power plants (WPPs) are usually concentrated in remote areas and unbalanced with load centers in terms of geographical distribution. The requirements for system operational stability and power transmission economics make large-scale wind power bundled with thermal power and transmitted to the loads by line-commutated converter based high-voltage direct current (LCC-HVDC) systems [1]. On the other hand, the permanent magnet synchronous generator (PMSG) has the advantages of high efficiency, high power density, and high reliability, which makes PMSGs a research hotspot in the field of wind power technology [2]. In such power systems, the dynamic interaction among synchronous generators (SGs), PMSGs, and LCC-HVDC system becomes complex. It is of practical engineering value to investigate the dynamic interaction mechanism and damping characteristic of wind-thermal-bundled power transmission by the LCC-HVDC system.

Until recently, the dynamic interaction between wind turbines (WTs) and AC grids has been extensively studied. It is found that the system instability occurs when the PMSGs are integrated with weak AC grids [3] - [6]. In [7], modal analysis is adopted to study the effect of WTs on power system small-signal stability. In [8], the WPP is modeled with individual WTs and the impact of individual WTs on the damping of the power oscillation is investigated based on the eigenvalue analysis. In [9], based on the participation factors, it is found that the electromechanical oscillation modes (EOMs) of the power system can be influenced by the outer-loop control of the PMSG reactive power, and the converter oscillation modes (COMs) of PMSGs are influenced by the SGs considerably. The dual participation of the PMSG and SG occurs when the COMs and EOMs have close frequencies [9]. In [10], it is shown that inertia control of WTs has an adverse impact on the damping of EOMs. In [11] and [12], it is pointed out that the modal resonance occurs when an open-loop EOM of the power system is close to an open-loop COM of the PMSG on the complex plane. For multiple PMSGs connected to a weak AC grid, eigenvalue analysis method, impedance-based analysis method, and time-domain simulation are used to reveal the sub-synchronous oscillation (SSO) mechanism [13].

For the dynamic interaction between the high-voltage direct current (HVDC) system and the AC grid, the effect of the controller parameters and the AC grid strength on the stability is investigated based on the eigenvalue analysis [14]. When the HVDC and the rest of the power system (ROPS)

Manuscript received: February 15, 2023; revised: April 27, 2023; accepted: June 9, 2023. Date of CrossCheck: June 9, 2023. Date of online publication: July 19, 2023.

This work was supported in part by the National Natural Science Foundation of China (No. U22B20109).

This article is distributed under the terms of the Creative Commons Attribution 4.0 International License (http://creativecommons.org/licenses/by/4.0/).

L. Zheng (corresponding author) and S. Ma are with the Power System Department, China Electric Power Research Institute, Beijing 100192, China (e-mail: 18713591731@163.com; msy_1969@163.com).

DOI: 10.35833/MPCE.2023.000094

have close open-loop SSO modes, the modal resonance occurs and the system stability degrades [15]. In [16]-[18], when an open-loop oscillation mode of the voltage source converter based high-voltage direct current (VSC-HVDC) and a torsional oscillation mode of the SG are close on the complex plane, the system stability is reduced. In [19] and [20], it is pointed out that the rectifier-side controller of the LCC-HVDC system provides the negative damping torque to the torsional system of a nearby SG.

However, previous studies in [3]-[20] are the two-device scenario. The three-device scenario, namely the SG, WT, and LCC-HVDC system, becomes more general. There are many studies about this type of grid such as [21]-[27]. It is pointed out that a doubly-fed induction generator (DFIG) connected to the LCC-HVDC system can support the system frequency [21], [22]. Considering the frequency coupling, the interaction among DFIG, LCC-HVDC system, and weak AC grid is studied using the impedance model [23]. Based on the strong mode resonance theory, the interaction among PMSG, AC grid, and LCC-HVDC system is studied in [24]. In [25], based on the closed-loop transfer function diagram, the transmission path of sub-synchronous frequency disturbance between PMSG and LCC-HVDC system is analyzed and the effect of the control parameters on SSO mode damping is presented. However, the external AC grid is equivalent to a voltage source and the dynamics of the thermal power unit are not considered [21]-[25]. Referring to [13], the torsional vibration of the SG shaft system was excited and the torsional vibration protection operated, which caused a serious SSO incident in the Hami grid, China on July 1, 2015. Thus, the dynamics of the SG need to be considered to further investigate the dynamic interaction among the PMSG, SG, and LCC-HVDC system.

In [26], based on the swing dynamic equation of the SG, the DFIG connected with the LCC-HVDC system in a weak AC grid is established as a four-order nonlinear model. The influence of frequency droop control of DFIGs and frequency control of LCC-HVDC systems on the synchronizing and damping torque of the rectifier-side generator is studied [26]. However, the frequency controllers of WTs and LCC-HVDC systems are different from the conventional double-loop control of WTs and the constant current control of the LCC-HVDC system. For wind-thermal-bundled power transmission by the LCC-HVDC system, explicit paths can explain how the interaction between the PMSG and LCC-HVDC system affects the total sub-synchronous torsional interaction (SSTI) damping of SGs [27]. Although the SG model with six windings and a mechanical subsystem is established to study the SSTI, the dynamic interaction of this three-device system is not clear for the EOM of SGs.

Eigenvalue analysis, impedance analysis, and time domain simulations are used to analyze the interaction mechanism in power systems. Eigenvalue analysis can provide the relevant variables for the oscillation modes, but the physical meaning of this method for the description of the dynamic interaction process among subsystems is unclear. The impedance analysis method describes the characteristics of the system based on an impedance model and evaluates the stability based on the impedance stability criterion. The impedance analysis is not suitable to reveal the disturbance transfer process. Time-domain simulations are used to verify the validity of other methods, which do not reveal dynamic interaction. Due to the limitations of the above methods, it is necessary to find a new method to analyze the interaction mechanisms and damping characteristics of wind-thermal-bundled power transmission by the LCC-HVDC system.

Compared with the above-mentioned methods, the path analysis method (PAM) can analyze the interaction mechanism through the closed-loop transfer function block diagram of the system, which has been used to investigate the SSO issue in [25], [28]-[31]. The process of PAM are as follows.

1) Based on the closed-loop transfer function block diagram, PAM can intuitively present the disturbance transfer process and the coupling relationship among subsystems.

2) Based on the dominant variables of the oscillation mode, the multi-input and multi-output (MIMO) transfer function matrix can be transformed into a single-input and single-output (SISO) transfer function by the damping construction method.

3) The damping coefficient can be used to quantify the stability of the oscillation mode.

Therefore, PAM is more explicit and practical to study the dynamic interaction and damping characteristics for wind-thermal-bundled power transmission by the LCC-HVDC system.

At present, various control strategies have been proposed to enhance system stability [32]-[37]. With the invariant control scheme, the small-signal stability can be improved based on the control parameter optimization. In terms of the dynamic performance, the error integral performance index (ITAE) is adopted to construct the objective function [34], [35]. Based on the eigenvalue sensitivity iterative method of the linearized state space model, the optimized control parameters are selected to improve the optimization efficiency [36], [37]. In [34]-[37], only the dominant modes are considered. However, the change in the parameters can lead to the migration of the dominant oscillation mode. In this paper, based on the small-signal model of the system, the penalty functions of oscillation modes and decay modes are used to construct the objective function, and the Monte Carlo method is adopted to solve the optimization problem.

For wind-thermal-bundled power transmission by LCC-HVDC systems, there are multiple oscillation modes. Among them, the SG-dominated oscillation mode is selected to investigate the interaction mechanism and coupling relationship based on the PAM in this paper. The effect of PMSG and LCC-HVDC system on the damping of SG-dominated oscillation modes is analyzed based on the damping reconstruction and eigenvalue method, respectively. The main contributions of this paper are as follows.

1) The linearized models (LMs) for the PMSG subsystem, LCC-HVDC subsystem, and SG subsystem are established, and the closed-loop transfer function block diagram of the system is obtained. The disturbance transfer path and coupling relationship among subsystems are revealed based on

the PAM. The damping characteristic of the system is studied based on the damping reconstruction method.

2) The small-signal model of wind-thermal-bundled power transmission by LCC-HVDC systems is established and the damping characteristic is analyzed based on eigenvalue analysis.

3) Based on the small-signal model, the penalty functions of oscillation modes and decay modes are used to construct the objective function. The parameter optimization problem is solved by the Monte Carlo method.

The rest of the paper is organized as follows. Based on the modular modeling, the LMs for the PMSG, LCC-HVDC, and SG subsystems are established in Section II. In Section III, the damping characteristic of the power system is analyzed based on the PAM and the eigenvalue analysis, respectively. In Section IV, the effect of the control parameters on the damping characteristic is presented. An optimization strategy based on Monte Carlo method is proposed to enhance the system stability in Section V. Finally, the conclusions are presented in Section VI.

II. LMs for PMSG, LCC-HVDC, and SG Subsystems

In this section, the LMs for the PMSG, LCC-HVDC, and SG subsystems are established based on the transfer function, and the accuracy of the LMs is verified.

The schematic diagram of the wind-thermal-bundled power transmission by LCC-HVDC systems is shown in Fig. 1. To reveal the dynamic interaction mechanisms, the whole system is divided into the PMSG subsystem, the SG subsystem, and the LCC-HVDC subsystem.

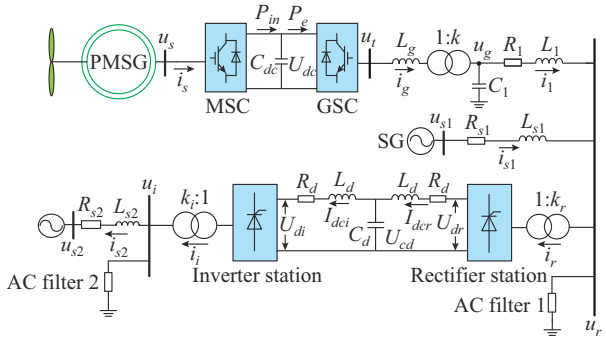

Fig. 1. Schematic diagram of wind-thermal-bundled power transmission by LCC-HVDC systems.

In the PMSG subsystem, u_s and i_s are the stator voltage and current of the WT, respectively; P_{in} is the output power of the machine-side converter (MSC); P_e is the input power of the grid-side converter (GSC); C_{dc} is the DC capacitance between the MSC and the GSC; U_{dc} is the DC voltage of the PMSG; L_g is the filter inductance; C_1 is the line capacitance; k is the transformer ratio of the grid-connected PMSG; u_t and i_g are the output voltage and current of the GSC, respectively; u_g is the voltage of the line capacitance; and R_1, L_1, and i_1 are the grid-side resistance, inductance, and current, respectively.

In the SG subsystem, u_{s1} and i_{s1} are the terminal voltage and output current of the SG, respectively; and R_{s1} and L_{s1} are the resistance and inductance of the transmission lines, respectively.

In the LCC-HVDC subsystem, R_d, L_d, and C_d are the DC resistance, inductance, and capacitance of the LCC-HVDC system, respectively; U_{cd} is the voltage of the DC capacitance; k_r and k_i are the transformer ratios of the rectifier and inverter side, respectively; U_{dr} and U_{di} are the DC voltages of the rectifier and inverter, respectively; I_{dcr} and I_{dci} are the DC currents of the rectifier and inverter, respectively; i_r and i_i are the AC currents of the rectifier and inverter sides, respectively; u_r and u_i are the AC voltages of the rectifier and inverter sides, respectively; R_{s2} and L_{s2} are the resistance and inductance of the receiving-end AC grid, respectively; and u_{s2} and i_{s2} are the voltage and current of the receiving-end AC grid, respectively.

For the wind-thermal-bundled power transmission by LCC-HVDC systems, there are four coordinate systems, including the d-q coordinate system of the PMSG, the polar coordinate system of the LCC-HVDC system, the d_2-q_2 coordinate system of the SG, and the x-y synchronous coordinate system of the AC grid. In the following, the subscripts d, q, $d2$, $q2$, x and y denote the components of the variable in the corresponding coordinate system, and the subscript 0 denotes the initial value of the variable.

A. Model for PMSG Subsystem

The WT of the PMSG system is completely decoupled from the electrical circuit of the AC grid. The electromagnetic and electromechanical dynamics of the WT and MSC have little influence on the dynamics of the power system, which means that the dynamics of the WT and MSC can be equivalent to a steady power source. Thus, the PMSG subsystem consists of the DC capacitance, GSC, phase-locked loop (PLL), filter inductance, and AC transmission line. The GSC adopts constant DC voltage control, and its control structure is given in Fig. 2.

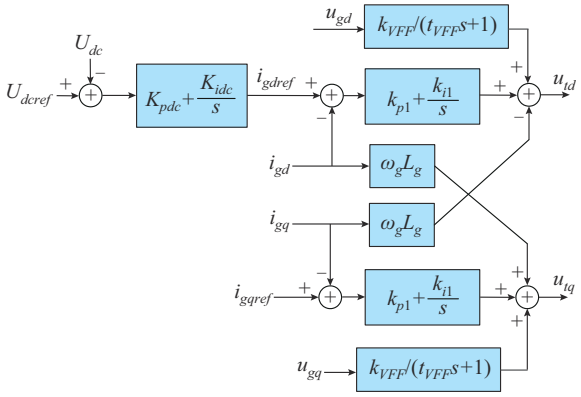

Fig. 2. Control structure of GSC.

In Fig. 2, U_{dcref} is the reference value of the DC voltage; ω_g is the controller frequency; i_{gdref} and i_{gqref} are the d- and q-axis components of reference outputs of the outer-loop control, respectively; K_{pdc} and K_{idc} are the proportional and integral coefficients of the DC voltage outer-loop control, respectively; k_{p1} and k_{i1} are the proportional and integral coefficients of the current inner-loop control, respectively; u_{td} and

u_{tq} are the d- and q-axis components of the GSC output voltage, respectively; u_{gd} and u_{gq} are the d- and q-axis components of the line capacitance voltage, respectively; i_{gd} and i_{gq} are the d- and q-axis components of the converter-side current, respectively; and $k_{VFF}/(t_{VFF}s+1)$ is a first-order filter for the voltage feedback.

The dynamics of the DC capacitance, GSC, and PLL are:

$$\begin{cases} \Delta U_{dc} = H_{dc}(s)\left(\Delta P_{in} - \Delta P_e\right) \\ \Delta P_e = 1.5\begin{bmatrix} u_{td0} & i_{gd0} & u_{tq0} & i_{gq0} \end{bmatrix}\begin{bmatrix} \Delta i_{gd} \\ \Delta u_{td} \\ \Delta i_{gq} \\ \Delta u_{tq} \end{bmatrix} \end{cases} \tag{1}$$

$$\begin{cases} \Delta i_{gdref} = H_{PI}(s)\Delta U_{dc} \\ \Delta i_{gqref} = 0 \end{cases} \tag{2}$$

$$\Delta\theta_{pll} = H_{pll}(s)\Delta u_{gq} \tag{3}$$

where $H_{dc}(s)$, $H_{PI}(s)$, and $H_{pll}(s)$ are the transfer functions of the DC capacitance, DC voltage outer-loop control, and PLL, respectively; and $\Delta\theta_{pll}$ is the PLL output angle.

The transfer functions in (1)-(3) are expressed as:

$$\begin{cases} H_{dc}(s) = \dfrac{1}{sC_{dc}U_{dc0}} \\ H_{PI}(s) = \dfrac{sK_{pdc}+K_{idc}}{s} \\ H_{pll}(s) = \dfrac{sk_{ppll}+k_{ipll}}{s^2} \end{cases} \tag{4}$$

where k_{ppll} and k_{ipll} are the proportional and integral coefficients of the PLL in the PMSG subsystem, respectively.

Considering the requirement to decouple the inner and outer loops of the controller, the bandwidth of the DC voltage outer loop is generally designed to be one-tenth of that of the inner loop. Therefore, it is believed that the current inner loop of the GSC allows the converter-side current to trace its reference value. It can be expressed as $\Delta i_{gd}=\Delta i_{gdref}$, $\Delta i_{gq}=\Delta i_{gqref}$. Since the power factor of the GSC is 1, Δi_{gqref} is set to be 0. Thus, Δi_{gq} and i_{gq} are equal to 0.

The dynamic equations for the filter inductance, line capacitance, and line impedance are given as:

$$\begin{bmatrix} \Delta u_{td} \\ \Delta u_{tq} \end{bmatrix} = \begin{bmatrix} \Delta u_{gd} \\ \Delta u_{gq} \end{bmatrix} + \begin{bmatrix} sL_g & -\omega_g L_g \\ \omega_g L_g & sL_g \end{bmatrix}\begin{bmatrix} \Delta i_{gd} \\ \Delta i_{gq} \end{bmatrix} \tag{5}$$

$$\begin{bmatrix} \Delta u_{gx} \\ \Delta u_{gy} \end{bmatrix} = \begin{bmatrix} G_{C1}(s) & G_{C2}(s) & -G_{C1}(s) & -G_{C2}(s) \\ -G_{C2}(s) & G_{C1}(s) & G_{C2}(s) & -G_{C1}(s) \end{bmatrix}\begin{bmatrix} \Delta i_{gx} \\ \Delta i_{gy} \\ \Delta i_{1x} \\ \Delta i_{1y} \end{bmatrix} \tag{6}$$

$$\begin{bmatrix} \Delta i_{1x} \\ \Delta i_{1y} \end{bmatrix} = \begin{bmatrix} G_{L1}(s) & G_{L2}(s) & G_{L3}(s) & G_{L4}(s) \\ -G_{L2}(s) & G_{L1}(s) & -G_{L4}(s) & G_{L3}(s) \end{bmatrix}\begin{bmatrix} \Delta u_{gx} \\ \Delta u_{gy} \\ \Delta u_{rx} \\ \Delta u_{ry} \end{bmatrix} \tag{7}$$

where the detailed expressions of transfer functions $G_{C1}(s)$, $G_{C2}(s)$, and $G_{L1}(s)$ - $G_{L4}(s)$ are given in (A1)-(A5) in Supplementary Material A.

The conversion equations between the corresponding components of $\Delta\boldsymbol{u}_g$ and $\Delta\boldsymbol{i}_g$ in the d-q coordinate system and x-y coordinate system are expressed as:

$$\begin{bmatrix} \Delta u_{gd} \\ \Delta u_{gq} \end{bmatrix} = k\begin{bmatrix} \cos\theta_0 & \sin\theta_0 & K_1 \\ -\sin\theta_0 & \cos\theta_0 & K_2 \end{bmatrix}\begin{bmatrix} \Delta u_{gx} \\ \Delta u_{gy} \\ \Delta\theta_{pll} \end{bmatrix} \tag{8}$$

$$\begin{bmatrix} \Delta i_{gx} \\ \Delta i_{gy} \end{bmatrix} = k\begin{bmatrix} \cos\theta_0 & -\sin\theta_0 & K_3 \\ \sin\theta_0 & \cos\theta_0 & K_4 \end{bmatrix}\begin{bmatrix} \Delta i_{gd} \\ \Delta i_{gq} \\ \Delta\theta_{pll} \end{bmatrix} \tag{9}$$

where θ_0 is the initial value of θ_{pll}; and the detailed expressions of K_1-K_4 are given in (A6) in Supplementary Material A.

Based on (6), (7), and (9), Δi_{1x} and Δi_{1y} are expressed as:

$$\begin{bmatrix} \Delta i_{1x} \\ \Delta i_{1y} \end{bmatrix} = \begin{bmatrix} G_{1x1}(s) & G_{1x2}(s) & G_{1x3}(s) & G_{1x4}(s) \\ G_{1y1}(s) & G_{1y2}(s) & G_{1y3}(s) & G_{1y4}(s) \end{bmatrix}\begin{bmatrix} \Delta i_{gd} \\ \Delta\theta_{pll} \\ \Delta u_{rx} \\ \Delta u_{ry} \end{bmatrix} \tag{10}$$

where $G_{1xi}(s)$ $(i=1,2,3,4)$ denotes the transfer functions from Δi_{gd}, $\Delta\theta_{pll}$, Δu_{rx}, and Δu_{ry} to Δi_{1x}, respectively; and $G_{1yi}(s)$ $(i=1,2,3,4)$ denotes the transfer functions from Δi_{gd}, $\Delta\theta_{pll}$, Δu_{rx}, and Δu_{ry} to Δi_{1y}, respectively.

Based on (6), (8), and (9), Δu_{gd} and Δu_{gq} are expressed as:

$$\begin{bmatrix} \Delta u_{gd} \\ \Delta u_{gq} \end{bmatrix} = \begin{bmatrix} G_{gd1}(s) & G_{gd2}(s) & G_{gd3}(s) & G_{gd4}(s) \\ G_{gq1}(s) & G_{gq2}(s) & G_{gq3}(s) & G_{gq4}(s) \end{bmatrix}\begin{bmatrix} \Delta i_{gd} \\ \Delta\theta_{pll} \\ \Delta i_{1x} \\ \Delta i_{1y} \end{bmatrix} \tag{11}$$

where $G_{gdi}(s)$ $(i=1,2,3,4)$ denotes the transfer functions from Δi_{gd}, $\Delta\theta_{pll}$, Δi_{1x}, and Δi_{1y} to Δu_{gd}, respectively; and $G_{gqi}(s)$ $(i=1,2,3,4)$ denotes the transfer functions from Δi_{gd}, $\Delta\theta_{pll}$, Δi_{1x}, and Δi_{1y} to Δu_{gq}, respectively.

According to (1)-(4) and (10), the grid-side current $\Delta\boldsymbol{i}_1$ is expressed as:

$$\begin{bmatrix} \Delta i_{1x} \\ \Delta i_{1y} \end{bmatrix} = \boldsymbol{Y}_{p1}(s)\Delta U_{dc} + \boldsymbol{Y}_{p2}(s)\begin{bmatrix} \Delta u_{rx} \\ \Delta u_{ry} \end{bmatrix} \tag{12}$$

where $\boldsymbol{Y}_{p1}(s)$ and $\boldsymbol{Y}_{p2}(s)$ are the transfer function matrices from ΔU_{dc} and $\Delta\boldsymbol{u}_r$ to $\Delta\boldsymbol{i}_1$, respectively.

According to (1)-(3), (5), (10), and (11), the transfer function block diagram of the PMSG is shown in Fig. 3.

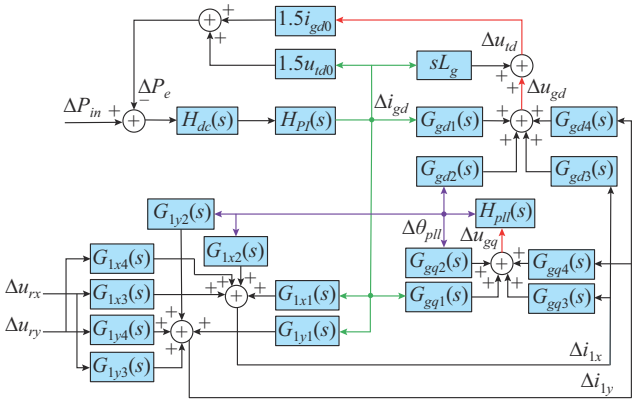

Fig. 3. Transfer function block diagram of PMSG.

In Fig. 3, the red lines denote the output paths of Δu_{gd}, Δu_{gq}, and Δu_{td}; the purple lines represent the paths directly related to $\Delta\theta_{pll}$; and the green lines are the paths directly related to Δi_{gd}.

B. Model for LCC-HVDC Subsystem

In the LCC-HVDC system, the rectifier operates in constant current control and the inverter operates in constant extinction angle control. On the LCC-HVDC rectifier side, the converter model, constant current controller, and PLL are considered. The control diagram of the LCC-HVDC rectifier is shown in Fig. 4.

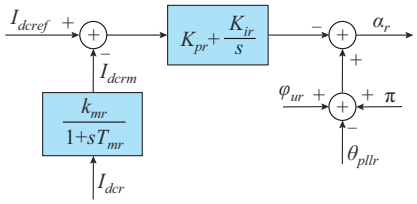

Fig. 4. Control diagram of LCC-HVDC rectifier.

In Fig. 4, I_{dcref} and I_{dcrm} are the reference and measured values of the DC current, respectively; $k_{mr}/(1+sT_{mr})$ is a first-order filter for current measurement; α_r is the actual firing angle of the rectifier; φ_{ur} is the phase angle of the AC bus voltage at the rectifier side; θ_{pllr} is the output angle of PLL in the rectifier; and K_{pr} and K_{ir} are the proportional and integral gains in the constant current controller, respectively.

The dynamic equations for the LCC-HVDC rectifier are expressed as:

$$\Delta I_{dcr}=\begin{bmatrix}-G_{1L}(s) & -G_{1L}(s) & G_{1L}(s) & G_{1L}(s)\end{bmatrix}\begin{bmatrix}\Delta\alpha_r\\ \Delta\varphi_{ur}\\ \Delta u_r\\ \Delta\theta_{pllr}\end{bmatrix} \tag{13}$$

$$\Delta\varphi_r=\begin{bmatrix}G_{2L}(s) & G_{3L}(s) & G_{4L}(s)\end{bmatrix}\begin{bmatrix}\Delta I_{dcr}\\ \Delta u_{rx}\\ \Delta u_{ry}\end{bmatrix} \tag{14}$$

$$\Delta\alpha_r=H_{dcr}(s)\Delta I_{dcr} \tag{15}$$

$$\Delta\theta_{pllr}=\begin{bmatrix}G_{5L}(s) & G_{6L}(s)\end{bmatrix}\begin{bmatrix}\Delta u_{rx}\\ \Delta u_{ry}\end{bmatrix} \tag{16}$$

where Δu_r and $\Delta\varphi_{ur}$ are the amplitude and angle of the PCC voltage, respectively; $\Delta\varphi_r$ is the power factor angle; $H_{dcr}(s)$ is the transfer function from ΔI_{dcr} to $\Delta\alpha_r$; and the detailed expressions of $G_{1L}(s)$-$G_{6L}(s)$ and $H_{dcr}(s)$ are given in (A13)-(A17) in Supplementary Material A.

Based on the conversion between the *x*-*y* coordinate system and the polar coordinate system, $\Delta\boldsymbol{i}_r$ and $\Delta\boldsymbol{u}_r$ are expressed as:

$$\begin{bmatrix}\Delta i_{rx}\\ \Delta i_{ry}\end{bmatrix}=\begin{bmatrix}K_5 & K_6 & K_7\\ K_8 & K_9 & K_{10}\end{bmatrix}\begin{bmatrix}\Delta I_{dcr}\\ \Delta\varphi_{ur}\\ \Delta\varphi_r\end{bmatrix} \tag{17}$$

$$\begin{bmatrix}\Delta u_r\\ \Delta\varphi_{ur}\end{bmatrix}=\begin{bmatrix}K_{11} & K_{12}\\ K_{13} & K_{14}\end{bmatrix}\begin{bmatrix}\Delta u_{rx}\\ \Delta u_{ry}\end{bmatrix} \tag{18}$$

where the detailed expressions of K_5-K_{14} are given in (A15) in Supplementary Material A.

By substituting (15), (16), and (18) into (13), (19) is obtained.

$$\Delta I_{dcr}=\begin{bmatrix}G_{Idc1}(s) & G_{Idc2}(s)\end{bmatrix}\begin{bmatrix}\Delta u_{rx}\\ \Delta u_{ry}\end{bmatrix} \tag{19}$$

where the detailed expressions of $G_{Idc1}(s)$ and $G_{Idc2}(s)$ are given in (A18) in Supplementary Material A.

By substituting (19) into (14) and eliminating ΔI_{dcr}, the power factor angle is calculated by:

$$\Delta\varphi_r=\begin{bmatrix}G_{\varphi r1}(s) & G_{\varphi r2}(s)\end{bmatrix}\begin{bmatrix}\Delta u_{rx}\\ \Delta u_{ry}\end{bmatrix} \tag{20}$$

where the detailed expressions of $G_{\varphi r1}(s)$ and $G_{\varphi r2}(s)$ are given in (A19) in Supplementary Material A.

By substituting (18)-(20) into (17), (21) is obtained.

$$\begin{bmatrix}\Delta i_{rx}\\ \Delta i_{ry}\end{bmatrix}=\boldsymbol{Y}_{LCC}(s)\begin{bmatrix}\Delta u_{rx}\\ \Delta u_{ry}\end{bmatrix} \tag{21}$$

where $\boldsymbol{Y}_{LCC}(s)$ is the transfer function matrix from $\Delta\boldsymbol{u}_r$ to $\Delta\boldsymbol{i}_r$, and its detailed expression is given in (A20) in Supplementary Material A.

According to (13)-(20), the transfer function block diagram of LCC-HVDC system is shown in Fig. 5.

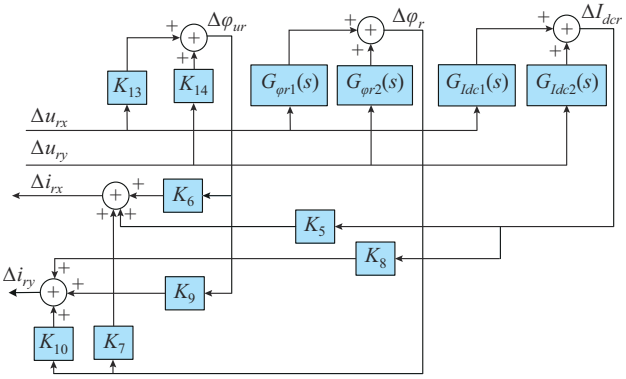

Fig. 5. Transfer function block diagram of LCC-HVDC system.

C. Model for SG Subsystem

In the d_2-q_2 coordinate system, the output current $\Delta\boldsymbol{i}_{s1}$ is expressed as:

$$\begin{bmatrix}\Delta i_{s1d2}\\ \Delta i_{s1q2}\end{bmatrix}=\begin{bmatrix}G_{SL1}(s) & G_{SL2}(s) & -G_{SL1}(s) & -G_{SL2}(s)\\ -G_{SL2}(s) & G_{SL1}(s) & G_{SL2}(s) & -G_{SL1}(s)\end{bmatrix}\begin{bmatrix}\Delta u_{s1d2}\\ \Delta u_{s1q2}\\ \Delta u_{rd2}\\ \Delta u_{rq2}\end{bmatrix} \tag{22}$$

where the detailed expressions of $G_{SL1}(s)$ and $G_{SL2}(s)$ are given in (A21) in Supplementary Material A.

The terminal voltage $\Delta\boldsymbol{u}_{s1}$ in the d_2-q_2 coordinate system is expressed as:

$$\begin{cases}\Delta u_{s1d2}=X_q\Delta i_{s1q2}\\ \Delta u_{s1q2}=\Delta E'_q-X'_d\Delta i_{s1d2}\end{cases} \tag{23}$$

where E'_q, X_q, and X'_d are the *q*-axis transient electromotive force voltage, *q*-axis reactance, and *d*-axis sub-transient reactance of SG, respectively.

The rotor swing equation for SG is:

$$\begin{cases} s\Delta\delta = \omega_0 \Delta\omega \\ s\Delta\omega = \dfrac{1}{M}\left(\Delta P_m - \Delta P_t - D\Delta\omega\right) \end{cases} \tag{24}$$

where $\Delta\delta$ is the power angle; $\Delta\omega$ is the rotor speed; ω_0 is synchronous speed; M is the inertia; D is the damping coefficient; and ΔP_m and ΔP_t are the mechanical power and electromagnetic power of SG, respectively.

By combining (22) and (23), (25) is obtained.

$$\begin{bmatrix} \Delta i_{s1d2} \\ \Delta i_{s1q2} \end{bmatrix} = \begin{bmatrix} G_{s1r}(s) & G_{s2r}(s) \\ G_{s3r}(s) & G_{s4r}(s) \end{bmatrix} \begin{bmatrix} \Delta u_{rd2} \\ \Delta u_{rq2} \end{bmatrix} \tag{25}$$

where the detailed expressions of $G_{s1r}(s)$-$G_{s4r}(s)$ are given in (A22) in Supplementary Material A.

The conversion equations between the corresponding components of $\Delta \boldsymbol{u}_r$ and $\Delta \boldsymbol{i}_{s1}$ in the d_2-q_2 coordinate system and the x-y coordinate system are:

$$\begin{bmatrix} \Delta u_{rd2} \\ \Delta u_{rq2} \end{bmatrix} = \begin{bmatrix} \cos\delta_0 & \sin\delta_0 & K_{15} \\ -\sin\delta_0 & \cos\delta_0 & K_{16} \end{bmatrix} \begin{bmatrix} \Delta u_{rx} \\ \Delta u_{ry} \\ \Delta\delta \end{bmatrix} \tag{26}$$

$$\begin{bmatrix} \Delta i_{s1d2} \\ \Delta i_{s1q2} \end{bmatrix} = \begin{bmatrix} \cos\delta_0 & \sin\delta_0 & K_{17} \\ -\sin\delta_0 & \cos\delta_0 & K_{18} \end{bmatrix} \begin{bmatrix} \Delta i_{s1x} \\ \Delta i_{s1y} \\ \Delta\delta \end{bmatrix} \tag{27}$$

where δ_0 is the initial value of δ; and the detailed expressions of K_{15}-K_{18} are given in (A23) in Supplementary Material A.

By combining (25)-(27), (28) is obtained.

$$\begin{bmatrix} \Delta i_{s1x} \\ \Delta i_{s1y} \end{bmatrix} = \boldsymbol{G}_{s1}(s) \begin{bmatrix} \Delta u_{rx} \\ \Delta u_{ry} \end{bmatrix} + \boldsymbol{G}_{s2}(s)\Delta\delta \tag{28}$$

where $\boldsymbol{G}_{s1}(s)$ and $\boldsymbol{G}_{s2}(s)$ are the transfer function matrices from $\Delta \boldsymbol{u}_r$ and $\Delta\delta$ to $\Delta \boldsymbol{i}_{s1}$, respectively. The detailed expressions of $\boldsymbol{G}_{s1}(s)$ and $\boldsymbol{G}_{s2}(s)$ are given in (A24) and (A25) in Supplementary Material A.

The electromagnetic power of SG is calculated by:

$$\Delta P_t = \begin{bmatrix} i_{s1d20} & i_{s1q20} & u_{s1d20} & u_{s1q20} \end{bmatrix} \begin{bmatrix} \Delta u_{s1d2} \\ \Delta u_{s1q2} \\ \Delta i_{s1d2} \\ \Delta i_{s1q2} \end{bmatrix} \tag{29}$$

By substituting (23) and (27) into (29), (30) is obtained.

$$\Delta P_t = \boldsymbol{H}_{pxy}(s) \begin{bmatrix} \Delta i_{s1x} \\ \Delta i_{s1y} \end{bmatrix} + H_{p\delta}(s)\Delta\delta \tag{30}$$

where $\boldsymbol{H}_{pxy}(s)$ is the transfer function matrix from $\Delta \boldsymbol{i}_{s1}$ to ΔP_t; and $H_{p\delta}(s)$ is the transfer function from $\Delta\delta$ to ΔP_t. The detailed expressions of $\boldsymbol{H}_{pxy}(s)$ and $H_{p\delta}(s)$ are given in (A26) in Supplementary Material A.

By substituting (28) into (30), (31) is obtained.

$$\Delta P_t = \boldsymbol{G}_{pxy}(s) \begin{bmatrix} \Delta u_{rx} \\ \Delta u_{ry} \end{bmatrix} + G_{p\delta}(s)\Delta\delta \tag{31}$$

where $\boldsymbol{G}_{pxy}(s)$ is the transfer function matrix from $\Delta \boldsymbol{u}_r$ to ΔP_t; and $G_{p\delta}(s)$ is the transfer function from $\Delta\delta$ to ΔP_t. The detailed expressions of $\boldsymbol{G}_{pxy}(s)$ and $G_{p\delta}(s)$ are given in (A27) in Supplementary Material A.

In the LCC-HVDC rectifier, the AC filter is equivalent to a capacitance, denoted by C_{g1}. The dynamic equation of the PCC bus is:

$$\begin{bmatrix} \Delta u_{rx} \\ \Delta u_{ry} \end{bmatrix} = \boldsymbol{G}_{PM}(s) \begin{bmatrix} \Delta i_{1x} \\ \Delta i_{1y} \end{bmatrix} + \boldsymbol{G}_{SG}(s) \begin{bmatrix} \Delta i_{s1x} \\ \Delta i_{s1y} \end{bmatrix} + \boldsymbol{G}_{LCC}(s) \begin{bmatrix} \Delta i_{rx} \\ \Delta i_{ry} \end{bmatrix} \tag{32}$$

where $\boldsymbol{G}_{PM}(s)$, $\boldsymbol{G}_{SG}(s)$, and $\boldsymbol{G}_{LCC}(s)$ are the transfer function matrices from $\Delta \boldsymbol{i}_1$, $\Delta \boldsymbol{i}_{s1}$, and $\Delta \boldsymbol{i}_r$ to $\Delta \boldsymbol{u}_r$, respectively. The detailed expressions of $\boldsymbol{G}_{PM}(s)$, $\boldsymbol{G}_{SG}(s)$, and $\boldsymbol{G}_{LCC}(s)$ are given in (A28) and (A29) in Supplementary Material A.

D. Validation of LMs

The complete LM is formed by interconnecting the dynamic models of each subsystem. Before analyzing the dynamic interaction mechanism, the accuracy of the LM in MATLAB/Simulink needs to be verified through the electromagnetic transient model (ETM) in DigSILENT/PowerFactory. The PMSG is subject to a step change of the DC voltage reference value U_{dcref} from 1.1 p.u. to 1.15 p.u. at $t = 0.6$ s. The system responses under the LM and the ETM are given in Fig. 6. In Fig. 6, the responses of the LM are consistent with those of the ETM, verifying the accuracy of the LM.

III. Damping Characteristic Analysis

In this section, the damping characteristic of the wind-thermal-bundled power transmission by the LCC-HVDC system is studied based on the PAM and the eigenvalue analysis method, respectively. In the PAM, the damping path and the disturbance transfer path are defined to reveal the dynamic interaction mechanism. Based on the damping decomposition method, the internal damping of SG and the interaction damping among subsystems are calculated. In the eigenvalue analysis, the small-signal model of the system and the results of the eigenvalue analysis are presented.

A. Damping Characteristic Analysis Based on PAM and Damping Reconstruction Method

In this subsection, the complete closed-loop transfer function block diagram of the system is derived. The damping path and the disturbance transfer path are defined, and each path is discussed in detail. Then, the internal damping characteristic of SG and the interaction damping characteristic among subsystems are separated based on the damping decomposition method.

1) Damping Path and Disturbance Transfer Path Analysis

In Fig. 3, the output power of PMSG is:

$$\Delta P_e = P_{e1}(s)\Delta U_{dc} + \boldsymbol{P}_{e2}(s) \begin{bmatrix} \Delta u_{rx} \\ \Delta u_{ry} \end{bmatrix} \tag{33}$$

where $P_{e1}(s)$ is the transfer function from ΔU_{dc} to ΔP_e; and $\boldsymbol{P}_{e2}(s)$ is the transfer function matrix from $\Delta \boldsymbol{u}_r$ to ΔP_e.

The open-loop transfer function block diagram of PMSG with input variable ΔP_{in} and output variable $\Delta \boldsymbol{i}_1$ is shown in Fig. 3. The transfer function block diagram of LCC-HVDC system with input variable $\Delta \boldsymbol{u}_r$ and output variable $\Delta \boldsymbol{i}_r$ is illustrated in Fig. 5. The transfer function block diagram of SG with input variable ΔP_m and output variable $\Delta \boldsymbol{i}_{s1}$ is obtained based on (24), (28), and (30).

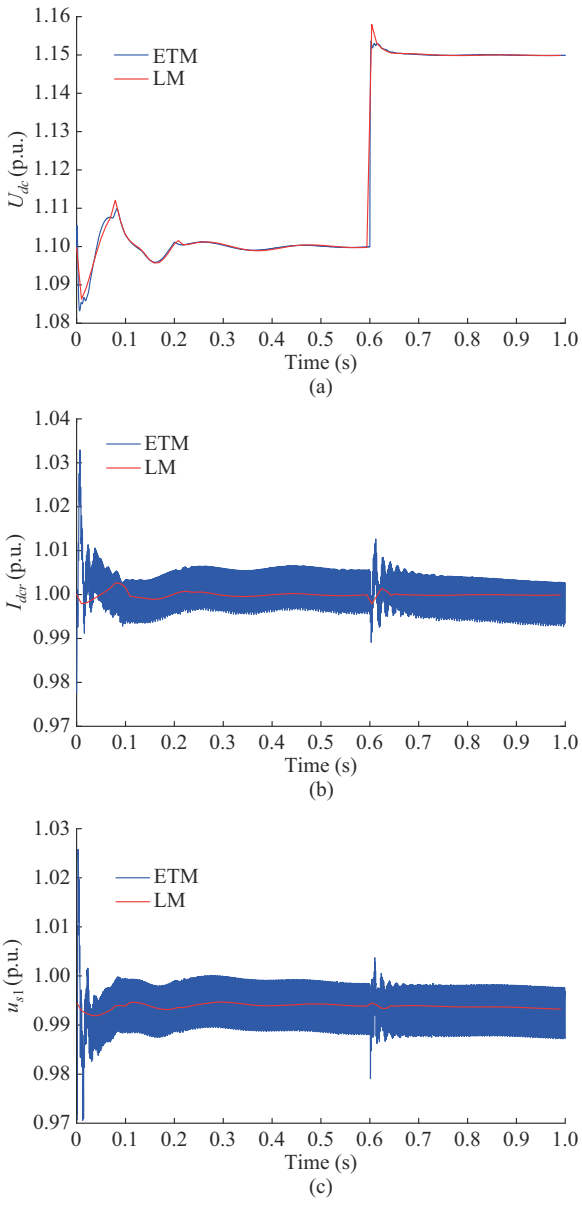

Fig. 6. System responses under LM and ETM. (a) U_{dc}. (b) I_{dcr}. (c) u_{s1}.

These three subsystems are interconnected by PCC, and the closed-loop transfer function block diagram of the wind-thermal-bundled power transmission by the LCC-HVDC system is shown in Fig. 7.

For the SG-dominated oscillation, the damping path is defined as the closed loop passing the rotor speed $\Delta\omega$ in the closed-loop transfer function block diagram. As shown in Fig. 7, there are two damping loops in the system, which are marked as closed loop 1 and closed loop 2. The arrow denotes the direction of disturbance transfer.

Closed loop 1 reflects the internal damping characteristic of SG. Closed loop 2 can reflect the damping characteristic of subsystem interactions. $\Delta \boldsymbol{i}_{s1}$ is related to the power angle $\Delta\delta$ and the PCC voltage $\Delta \boldsymbol{u}_r$. When the PCC voltage $\Delta \boldsymbol{u}_r$ is disturbed, the output current of PMSG $\Delta \boldsymbol{i}_1$, the rectifier current of LCC-HVDC system $\Delta \boldsymbol{i}_r$, and the grid current of SG $\Delta \boldsymbol{i}_{s1}$ are disturbed. Meanwhile, $\Delta \boldsymbol{i}_1$, $\Delta \boldsymbol{i}_r$, and $\Delta \boldsymbol{i}_{s1}$ affect the PCC voltage $\Delta \boldsymbol{u}_r$. In this process, the parameters of each subsystem affect the disturbance transfer. Thus, the interaction among subsystems can be represented as a process of current disturbance and voltage disturbance driving each other at the PCC. The transmission channels of the oscillation disturbance in the path of the closed-loop transfer function block diagram are defined as the disturbance transfer paths, which reveal the disturbance transfer process and the coupling relationship among subsystems.

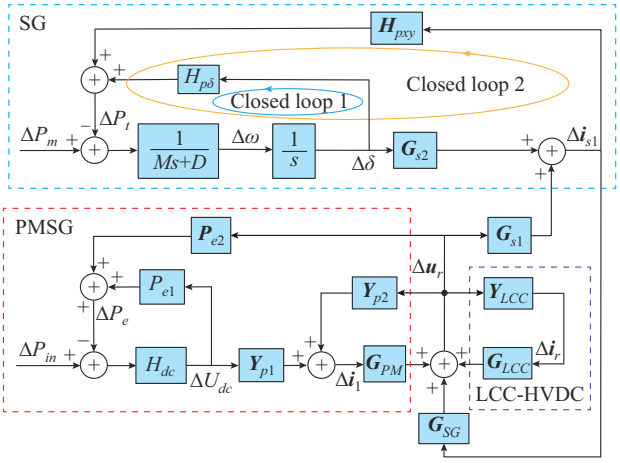

Fig. 7. Closed-loop transfer function block diagram of wind-thermal-bundled power transmission by LCC-HVDC system.

2) Theoretical Derivation of Damping Decomposition

Based on the results of the path analysis, the total damping of SG is determined by the internal characteristic of SG and the interaction characteristic among subsystems. It is essential to decompose the total damping of SG.

In this part, based on the damping decomposition method, the transfer function for each damping path is obtained and the damping coefficients corresponding to different damping characteristics are calculated. The detailed analysis is as follows.

Step 1: the MSC and GSC of PMSG are decoupled through the DC capacitance. The WT and MSC can be equivalent to a steady power source, i.e., $\Delta P_{in}=0$. By combining (1) and (33), (34) and Fig. 8(a) are obtained.

$$\Delta U_{dc}=\frac{-H_{dc}(s)\boldsymbol{P}_{e2}(s)}{1+H_{dc}(s)P_{e1}(s)}\Delta \boldsymbol{u}_r=\boldsymbol{G}_{d\text{-}ur}(s)\Delta \boldsymbol{u}_r \tag{34}$$

Step 2: paths related to the PMSG and LCC-HVDC system are expressed by transfer function matrices $\boldsymbol{G}_a(s)$ and $\boldsymbol{G}_b(s)$, respectively, which are shown in (35) and Fig. 8(b).

$$\begin{cases}\boldsymbol{G}_a(s)=\boldsymbol{G}_{PM}(s)\big(\boldsymbol{Y}_{P1}(s)\boldsymbol{G}_{d\text{-}ur}(s)+\boldsymbol{Y}_{P2}(s)\big)\\ \boldsymbol{G}_b(s)=\boldsymbol{G}_{LCC}(s)\boldsymbol{Y}_{LCC}(s)\end{cases} \tag{35}$$

Step 3: in Fig. 8(b), the relationship between the SG output current $\Delta \boldsymbol{i}_{s1}$ and the PCC voltage $\Delta \boldsymbol{u}_r$ is expressed by:

$$\Delta \boldsymbol{i}_{s1}=\boldsymbol{G}_{SG}^{-1}(s)\big(\boldsymbol{I}-\boldsymbol{G}_a(s)-\boldsymbol{G}_b(s)\big)\Delta \boldsymbol{u}_r=\boldsymbol{G}_c(s)\Delta \boldsymbol{u}_r \tag{36}$$

By combining (28) and (36), (37) and Fig. 8(c) are obtained.

$$\Delta \boldsymbol{u}_r=\big(\boldsymbol{G}_c(s)-\boldsymbol{G}_{s1}(s)\big)^{-1}\boldsymbol{G}_{s2}(s)\Delta\delta=\boldsymbol{G}_d(s)\Delta\delta \tag{37}$$

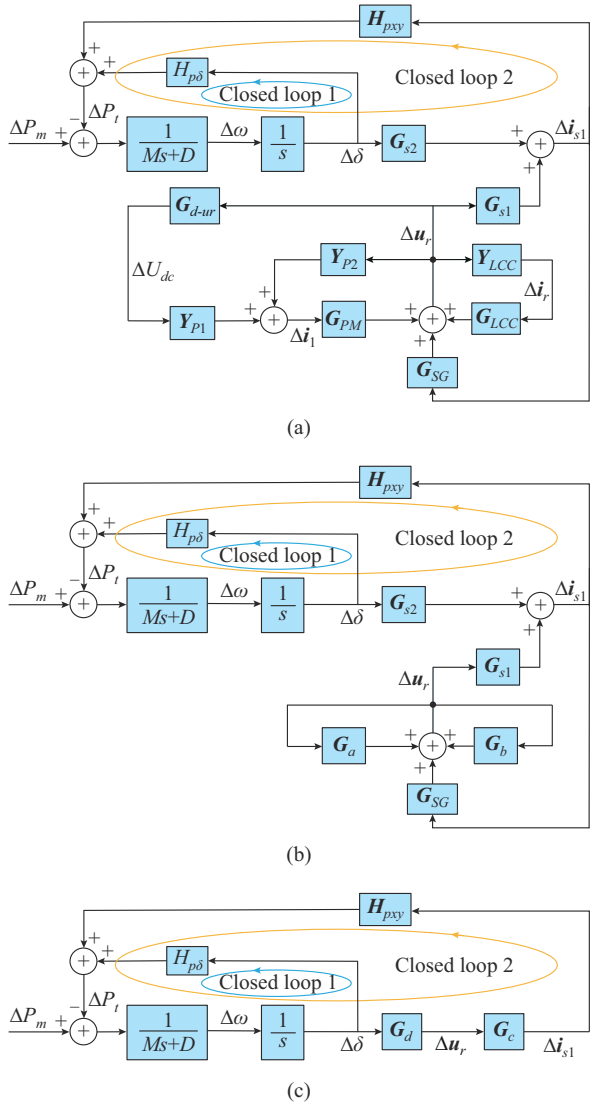

Fig. 8. Theoretical derivation of damping decomposition. (a) Introduction of $\boldsymbol{G}_{d\text{-}ur}(s)$. (b) Introduction of $\boldsymbol{G}_a(s)$ and $\boldsymbol{G}_b(s)$. (c) Introduction of $\boldsymbol{G}_c(s)$ and $\boldsymbol{G}_d(s)$.

The internal damping characteristic of SG and the interaction damping characteristic among subsystems are denoted by $K_{d1}(s)$ and $K_{d2}(s)$, respectively; and $K_d(s)$ is defined as the sum of the damping characteristics, as shown in (38).

$$\begin{cases} K_{d1}(s) = H_{p\delta}(s) \\ K_{d2}(s) = \boldsymbol{H}_{pxy}(s)\boldsymbol{G}_c(s)\boldsymbol{G}_d(s) \\ K_d(s) = K_{d1}(s) + K_{d2}(s) \end{cases} \tag{38}$$

Based on the definition of the damping coefficient [30] and transfer functions in (38), the internal damping coefficient Z_1 and the interaction damping coefficient Z_2 can be obtained for SG. The total damping of SG is $Z = Z_1 + Z_2$.

B. Damping Characteristic Analysis Based on Eigenvalue Analysis Method

In this subsection, the small-signal model for the wind-thermal-bundled power transmission by the LCC-HVDC system is derived and the eigenvalue analysis results are presented.

1) Small-signal Model

The state equations for PMSG, SG, and LCC-HVDC subsystems have been extensively studied, and are not the focus of this paper. The detailed modeling processes of these subsystems can be found in [38], [39]. The state equation of the system with 22 state variables and 3 input variables is:

$$\begin{cases} \dfrac{\mathrm{d}\Delta\boldsymbol{x}_{sim}}{\mathrm{d}t} = \boldsymbol{A}_{sim}\Delta\boldsymbol{x}_{sim} + \boldsymbol{B}_{sim}\Delta\boldsymbol{u}_{sim} \\ \boldsymbol{x}_{sim} = \left[\delta, \omega, i_{s1d2}, i_{s1q2}, x_1, x_a, \theta_{pllr}, I_{dcr}, u_{rx}, u_{ry}, \right. \\ \qquad \left. U_{dc}, x_2, x_3, x_4, x_b, \theta_{pll}, i_{gd}, i_{gq}, u_{gd}, u_{gq}, i_{1d}, i_{1q}\right] \\ \boldsymbol{u}_{sim} = \left[U_{dcref} \quad I_{gqref} \quad I_{dcref}\right] \end{cases} \tag{39}$$

where $\boldsymbol{x}_{sim}$ is the state-variable vector; $\boldsymbol{A}_{sim}$ is the state matrix; $\boldsymbol{B}_{sim}$ is the input matrix; and $\boldsymbol{u}_{sim}$ is the input vector. In $\boldsymbol{x}_{sim}$, $\mathrm{d}x_1/\mathrm{d}t = I_{dcref} - I_{dcrm}$; $\mathrm{d}x_a/\mathrm{d}t = u_r$; $\mathrm{d}x_b/\mathrm{d}t = u_{gq}$; $\mathrm{d}\theta_{pllr}/\mathrm{d}t = \omega_0 + k_{pPLL}u_r + k_{iPLL}x_a$, and k_{pPLL} and k_{iPLL} are the proportional and integral coefficients of the PLL in the LCC-HVDC rectifier, respectively; $\mathrm{d}x_2/\mathrm{d}t = U_{dc} - U_{dcref}$; $\mathrm{d}x_3/\mathrm{d}t = i_{gdref} - i_{gd}$; $\mathrm{d}x_4/\mathrm{d}t = i_{gqref} - i_{gq}$; and $\mathrm{d}\theta_{pll}/\mathrm{d}t = \omega_0 + k_{ppll}u_{gq} + k_{ipll}x_b$.

2) Eigenvalue Analysis Results

Based on the small-signal model (39) and parameters in Table SAI in Supplementary Material A, the main oscillation modes of the system are shown in Table I.

TABLE I
OSCILLATION MODES OF WIND-THERMAL-BUNDLED POWER TRANSMISSION BY LCC-HVDC SYSTEM

Oscillation mode	Eigenvalue	Oscillation frequency (Hz)	Damping ratio
$\lambda_{1,2}$	$-78.33 \pm \mathrm{j}245.69$	39.1022	0.3038
$\lambda_{3,4}$	$-3.14 \pm \mathrm{j}12.79$	2.0365	0.2383
$\lambda_{5,6}$	$-80.25 \pm \mathrm{j}601.62$	95.7506	0.1322

As shown in Table I, there are three oscillation modes, including one SSO mode $\lambda_{1,2}$, one low-frequency oscillation (LFO) mode $\lambda_{3,4}$, and one medium-frequency oscillation mode $\lambda_{5,6}$. Based on the participation factor analysis, the mode $\lambda_{3,4}$ is related to the rotor speed of SG. And the mode $\lambda_{3,4}$ is closest to the imaginary axis and plays a dominant role in the stability, so the mode $\lambda_{3,4}$ is selected to analyze the damping characteristic of the system. The frequency range of the oscillation mode $\lambda_{3,4}$ is consistent with that of the damping reconstruction method.

Eigenvalue analysis can provide the variables associated with the oscillation modes, but the disturbance transfer path cannot be reflected by these variables. The PAM based on the closed-loop transfer function block diagram has the advantage of demonstrating the disturbance transfer process. Besides, the MIMO transfer function matrix is transformed into an SISO transfer function by damping reconstruction, and the damping of oscillation modes is evaluated. Therefore, PAM is more suitable for the interaction mechanisms analysis and damping characteristic analysis.

IV. Effect of Control Parameters on Damping Characteristics

In this section, the effect of the control parameters on the damping characteristics is investigated and the conclusions are verified by time-domain simulation results.

A. GSC Outer-loop Proportional Coefficient K_{pdc}

The effect of K_{pdc} on the damping characteristic is analyzed. The frequency characteristic curves of the interaction damping Z_2 with varying K_{pdc} are shown in Fig. 9(a) and the damping ratios of the oscillation mode $\lambda_{3,4}$ with varying K_{pdc} are shown in Fig. 9(b), where the arrows indicate the damping trends as K_{pdc} increases.

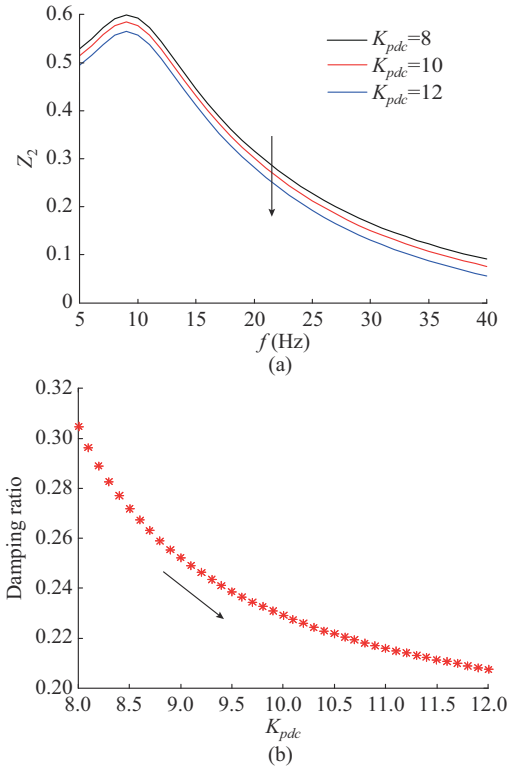

Fig. 9. Damping characteristic analysis results with varying K_{pdc}. (a) Damping coefficient calculated by PAM. (b) Damping ratio calculated by eigenvalue analysis.

In Fig. 9, the frequency characteristic curves of the interaction damping Z_2 move downward and the damping ratio decreases with the increase of K_{pdc}, corresponding to a decrease in damping.

A three-phase short-circuit fault occurs at the high voltage (HV) bus of the PMSG at $t=0.4$ s and lasts for 0.01 s. The response curves of the SG active power with varying K_{pdc} are shown in Fig. 10.

In Fig. 10, the amplitude of the power oscillation increases and the system stability decreases as the K_{pdc} increases, verifying the correctness of the damping characteristic analysis.

B. GSC Outer-loop Integral Coefficient K_{idc}

The effect of K_{idc} on the damping is analyzed.

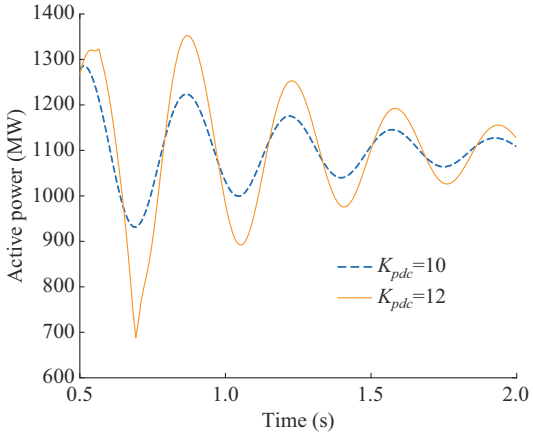

Fig. 10. Response curves of SG active power with varying K_{pdc}.

The frequency characteristic curves of the interaction damping Z_2 with varying K_{idc} are shown in Fig. 11(a) and the damping ratios of the oscillation mode $\lambda_{3,4}$ with varying K_{idc} are shown in Fig. 11(b), where the arrows represent the damping trends as K_{idc} increases.

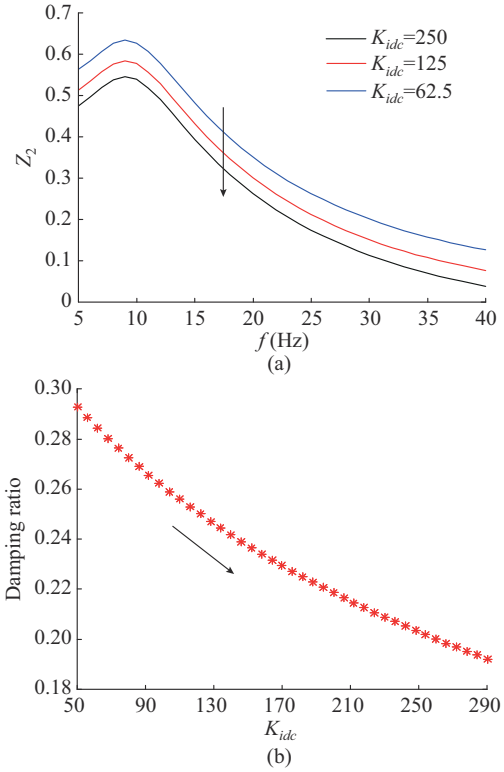

Fig. 11. Damping characteristic analysis results with varying K_{idc}. (a) Damping coefficient calculated by PAM. (b) Damping ratio calculated by eigenvalue analysis.

In Fig. 11, the frequency characteristic curves of the interaction damping Z_2 move downward and the damping ratio decreases with the increase of K_{idc}, corresponding to a decrease in damping.

With the same short-circuit fault in Section IV-A, Fig. 12 shows the response curves of the SG active power with varying K_{idc}. In Fig. 12, the amplitude of the power oscillation increases and the system stability decreases when K_{idc} increas-

es, which is consistent with the damping characteristic analysis results.

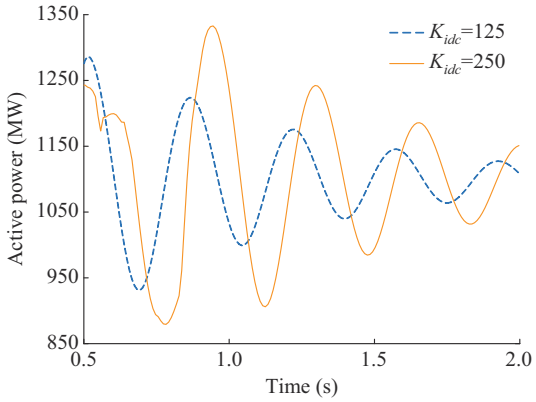

Fig. 12. Response curves of SG active power with varying K_{idc}.

C. Proportional Coefficient of LCC-HVDC Constant Current Control K_{pr}

The effect of K_{pr} on the damping characteristic is analyzed. The frequency characteristic curves of the interaction damping Z_2 with varying K_{pr} are shown in Fig. 13(a) and the damping ratios of the oscillation mode $\lambda_{3,4}$ with varying K_{pr} are shown in Fig. 13(b), where the arrows represent the damping trends as K_{pr} increases.

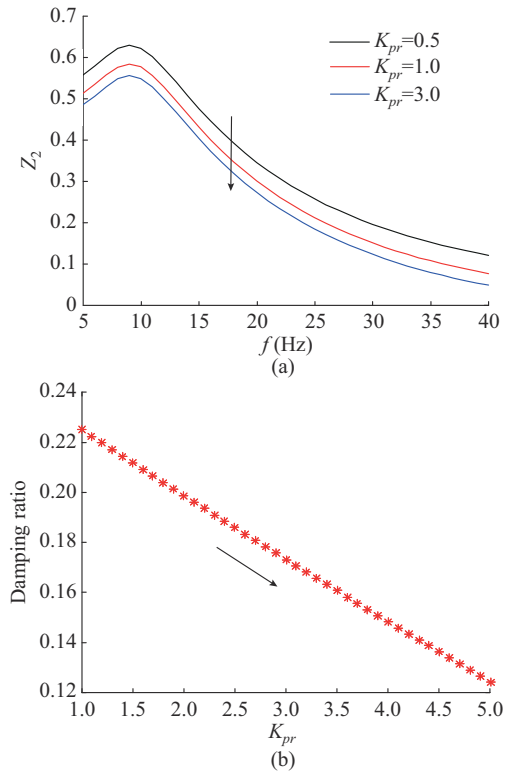

Fig. 13. Damping characteristic analysis results with varying K_{pr}. (a) Damping coefficient calculated by PAM. (b) Damping ratio calculated by eigenvalue analysis.

In Fig. 13, the frequency characteristic curves of the interaction damping Z_2 move downward and the damping ratio decreases with the increase of K_{pr}, corresponding to a decrease in damping.

With the same short-circuit fault in Section IV-A, Fig. 14 shows the response curves of the SG active power with varying K_{pr}.

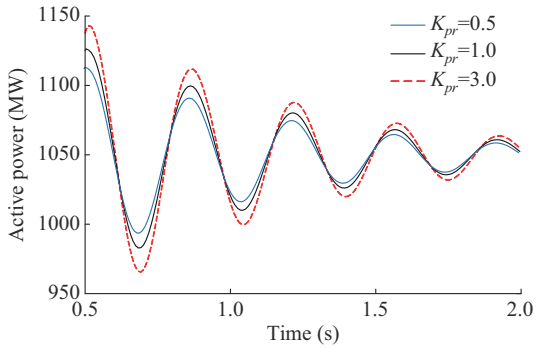

Fig. 14. Response curves of SG active power with varying K_{pr}.

In Fig. 14, the amplitude of the power oscillation increases and the system stability decreases when K_{pr} increases, which is consistent with the damping characteristic analysis results.

D. Integral Coefficient of LCC-HVDC Constant Current Control K_{ir}

The effect of K_{ir} on the damping characteristic is analyzed. The frequency characteristic curves of the interaction damping Z_2 with varying K_{ir} are shown in Fig. 15(a) and the damping ratios of the oscillation mode $\lambda_{3,4}$ with varying K_{ir} are shown in Fig. 15(b), where the arrows indicate the damping trend as K_{ir} increases.

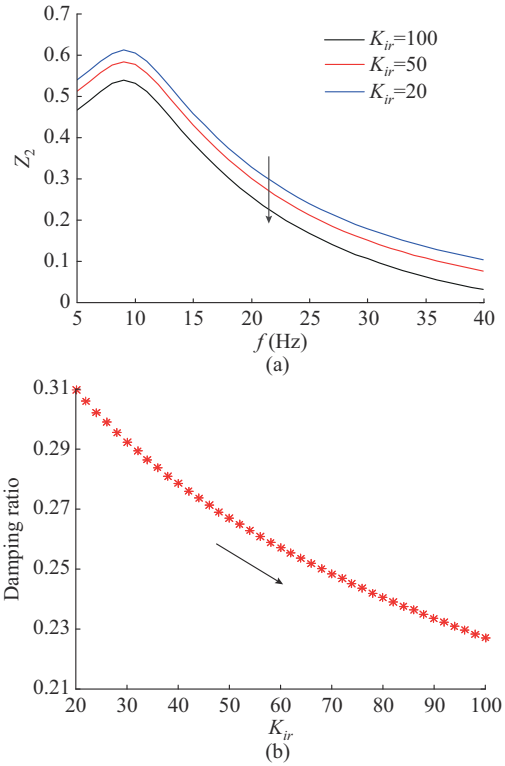

Fig. 15. Damping characteristic analysis results with varying K_{ir}. (a) Damping coefficient calculated by PAM. (b) Damping ratio calculated by eigenvalue analysis.

In Fig. 15, the damping characteristic curves of the interaction damping Z_2 move downward and the damping ratio decreases with the increase of K_{ir}, corresponding to a decrease in damping.

With the same short-circuit fault in Section IV-A, Fig. 16 shows the response curves of the SG active power with varying K_{ir}.

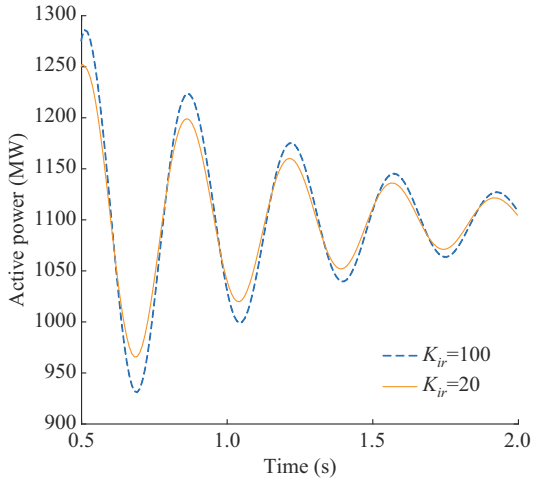

Fig. 16. Response curves of SG active power with varying K_{ir}.

In Fig. 16, the amplitude of the power oscillation increases and the system stability decreases when K_{ir} increases, verifying the correctness of the damping characteristic analysis.

V. Optimization Strategy Based on Monte Carlo Method

In this section, first, the objective function is constructed based on the penalty functions of the oscillation modes and decay modes. Then, the feasible optimization regions of the control parameters are obtained to ensure the small-signal stability of the system. Finally, the optimization problem is solved by Monte Carlo method and the effectiveness of the proposed strategy is verified by time-domain simulations.

A. Objective Function for Control Parameter Optimization

Constrained by the small-signal stability of the system, the system is assumed to have i complex eigenvalues and j real eigenvalues. Complex eigenvalues correspond to oscillation modes and their damping ratios reflect the decay rate of the oscillation. The real eigenvalues correspond to the decay modes. The designed objective function should keep all the real eigenvalues in the left half plane and away from the imaginary axis, and improve the damping ratios of complex eigenvalues.

The desired damping ratio of the oscillation mode and the desired value of the decay mode can be predefined. The redundancy between the desired value and the actual value is taken as an objective function. Besides, the weighted method is introduced to quantify the effect of different eigenvalues on the objective function. The objective function is constructed as:

$$\begin{cases} \min F = \sum_{k=1}^{i} \alpha_k P^{\lambda_{\alpha,k}} + \sum_{k=i+1}^{i+j} \beta_k P^{\lambda_{r,k}} \\ \text{s.t.} \left| (\sigma_k + \mathrm{j}\omega_k) \boldsymbol{E} - \boldsymbol{A}_{sim} \right| = 0 \quad k = 1, 2, \ldots, i+j \\ \varepsilon_k = -\dfrac{\sigma_k}{\sqrt{\sigma_k^2 + \omega_k^2}} \quad k = 1, 2, \ldots, i \\ \sigma_k < 0 \quad k = 1, 2, \ldots, i+j \end{cases} \tag{40}$$

where $\sigma_k + \mathrm{j}\omega_k$ is the k^{th} eigenvalue of the system; $\boldsymbol{E}$ is an identity matrix of the same order as $\boldsymbol{A}_{sim}$; ε_k is the damping ratio of the k^{th} oscillation mode; α_k and β_k are the weights of the two penalty functions, whose magnitudes are determined by the damping ratio and the distance between the eigenvalue and the imaginary axis, respectively; and $P^{\lambda_{\alpha,k}}$ and $P^{\lambda_{r,k}}$ are the penalty functions of the k^{th} oscillation mode and the k^{th} decay mode, respectively. The closer to the imaginary axis or the smaller the damping ratio, the larger the weight and the larger the penalty are.

The penalty function $P^{\lambda_{\alpha,k}}$ for the k^{th} oscillation mode is:

$$P^{\lambda_{\alpha,k}} = \begin{cases} 0 & \varepsilon_k \le \varepsilon_d \\ \varepsilon_d - \varepsilon_k & \text{else} \end{cases} \tag{41}$$

where ε_d is the desired damping ratio of the oscillation mode.

The penalty function $P^{\lambda_{r,k}}$ for the k^{th} decay mode is:

$$P^{\lambda_{r,k}} = \begin{cases} 0 & \sigma_k \le \sigma_d \\ \sigma_d - \sigma_k & \text{else} \end{cases} \tag{42}$$

where σ_d is the desired value of the decay mode.

B. Feasible Domain of Control Parameter

In the optimization process, the range of the parameters needs to be determined for the stability. According to the established small-signal model (39), the feasible optimization regions for the control parameters are obtained based on the root locus method.

Let the GSC outer-loop proportional coefficient K_{pdc} gradually increase from 1 to 25, whereas the other control parameters remain unchanged. The trajectory of the oscillation mode $\lambda_{3,4}$ with varying K_{pdc} is shown in Fig. 17, where the arrows represent the trend of $\lambda_{3,4}$ as K_{pdc} increases.

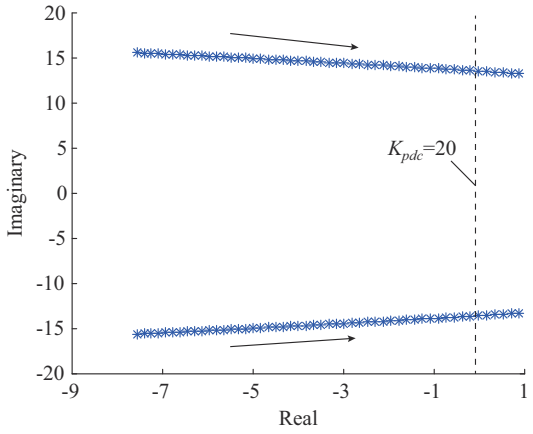

Fig. 17. Trajectory of oscillation mode $\lambda_{3,4}$ with varying K_{pdc}.

In Fig. 17, the increase of K_{pdc} can reduce the small-signal

stability of the system. $K_{pdc}=20$ is the critical parameter for system stability.

The influence of other control parameters on the oscillation mode $\lambda_{3,4}$ is analyzed in turn with a similar analysis method. The feasible optimization regions for the control parameters are shown in Table II, which are the constraints of the optimization problem.

TABLE II
FEASIBLE OPTIMIZATION REGIONS FOR CONTROL PARAMETERS

Control parameter	Feasible optimization region
K_{pdc}	$1 \le K_{pdc} \le 20$
K_{idc}	$50 \le K_{idc} \le 300$
K_{pr}	$0.1 \le K_{pr} \le 5$
K_{ir}	$10 \le K_{ir} \le 150$

C. Optimization of Control Parameters Based on Monte Carlo Method

The Monte Carlo method is a numerical computation method based on the theory of random numbers and probability statistics. The relationship between the eigenvalues and the parameters is difficult to formulate, so the Monte Carlo method is more suitable to solve the optimization problem of the control parameters. In the optimization process, the Monte Carlo method can transform complex multi-group control parameter optimization problems into the computation of random numbers and their digital characteristics, which significantly reduces the computational burden.

The basic idea of the optimization is as follows.

Step 1: calculate the value of the objective function with the initial control parameters.

Step 2: a new set of control parameters is randomly generated in the feasible optimization region of Table II, and the objective function value F_n corresponding to this set of parameters is calculated.

Step 3: repeat *Step 2*.

Step 4: the set of control parameters with the minimum value of the objective function is selected as the optimal parameters.

Figure 18 shows the flow chart of the optimization strategy based on the Monte Carlo method, and the steps are as follows.

Step 1: initialization. Based on the Monte Carlo method, a set of random numbers is generated in the feasible optimization region and the corresponding values are assigned to control parameters K_{pdc}, K_{idc}, K_{pr}, and K_{ir}. h_i $(i=1,2,3,4)$ represents the control parameters; n $(0<n<N_{\max})$ is the iteration number; $N_{\max}$ is set to be 10000; and *temp* is an intermediate variable used to compare the value of the objective function during the optimization process, with an initial value of 10^6.

Step 2: based on Monte Carlo method, the control parameters are updated with $h_i=h_{i\min}+R(h_{i\max}-h_{i\min})$, where R is a random number between 0 and 1, and $h_{i\max}$ and $h_{i\min}$ are the upper and lower limits of the control parameters in Table II, respectively. After updating the control parameter h_i, a new set of control parameters is generated. Calculate the value of the objective function F_n corresponding to the new parameter and perform *Step 3*.

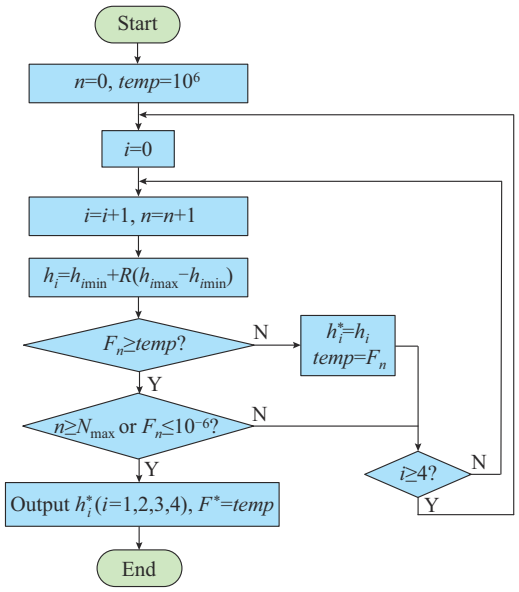

Fig. 18. Flow chart of optimization strategy based on Monte Carlo method.

Step 3: determine if F_n is greater than *temp*. If yes, go to *Step 4*. Otherwise, assign F_n to *temp* and assign this set of control parameters to the optimized control parameters h_i^*.

Step 4: determine if the iteration of the four parameters is complete, i.e., if i is greater than or equal to 4. If yes, perform *Step 2*; otherwise, perform *Step 3*.

Step 5: determine if n is greater than or equal to 10000, i.e., if the optimization process is completed, or if the value of the objective function F_n is less than 10^6. If yes, output h_i^* as the optimized parameter and output *temp* as the minimum value of the objective function F^*. Otherwise, perform *Step 4*.

The initial and optimized control parameters are shown in Table III by performing the above optimization steps.

TABLE III
INITIAL AND OPTIMIZED CONTROL PARAMETERS

Value	K_{pdc}	K_{idc}	K_{pr}	K_{ir}
Initial	10.00	125.00	1.00	100.00
Optimized	8.30	59.89	0.74	29.41

D. Verification of Optimized Result

To verify the effectiveness of the proposed strategy, the wind-thermal-bundled power transmission by the LCC-HVDC system before and after optimization is compared. A short-circuit fault occurs at the PMSG HV bus at $t=0.4$ s and lasts for 0.01 s. The dynamic response curves of the LCC-HVDC system before and after the optimization are shown in Fig. 19.

In Fig. 19, it is shown that the proposed strategy can significantly reduce the oscillation amplitude and shorten the settling time.

VI. Conclusion

In this paper, the dynamic interaction mechanism of the wind-thermal-bundled power transmission by LCC-HVDC systems is studied based on PAM, and damping characteristic analysis of SG-dominated oscillation mode is investigated based on the damping reconstruction method and the eigenvalue analysis, respectively. An optimization strategy based on Monte Carlo method is proposed. The main conclusions are drawn as follows.

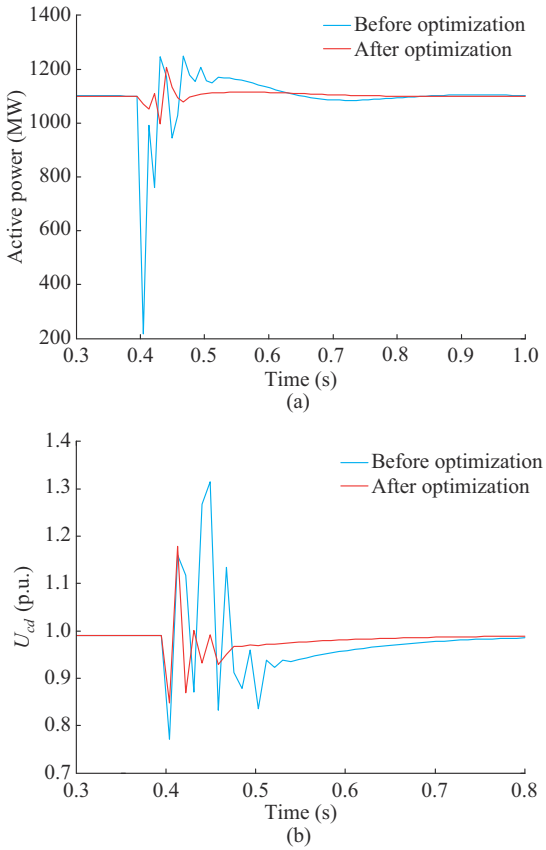

Fig. 19. Dynamic response curves of LCC-HVDC system before and after optimization. (a) Active power of SG. (b) DC voltage of LCC-HVDC system.

1) The LMs for the PMSG, LCC-HVDC system, and SG are established, and the accuracy of the complete dynamic model is verified by the ETM in DIgSILENT/PowerFactory.

2) Based on the PAM, the disturbance transfer path and coupling relationship among subsystems are revealed intuitively. For SG-dominated oscillation, the dynamic interaction among subsystems can be expressed as a dynamic process where current disturbance and voltage disturbance at the PCC drive each other. Based on the damping reconstruction, the total damping is decomposed into the internal damping of SG and the interaction damping among subsystems.

3) The small-signal model of the wind-thermal-bundled power transmission by LCC-HVDC systems is derived and the eigenvalue analysis results are presented.

4) The damping of the SG-dominated oscillation mode is negatively correlated with the GSC outer-loop proportional and integral coefficients. Meanwhile, the damping is negatively correlated with the proportional and integral coefficients of the LCC-HVDC constant current controller.

5) The penalty functions of oscillation modes and decay modes are used to construct the objective function and the proposed strategy based on Monte Carlo method can enhance the system stability.

References

[1] Y. Zhao, G. Yan, Z. Wang *et al*., "Analysis of subsynchronous torsional vibration of wind-thermal bundling delivery system via LCC-HVDC," in *Proceedings of 2023 IEEE 6th International Electrical and Energy Conference (CIEEC)*, Hefei, China, May 2023, pp. 1139-1144.

[2] H. Liu, X. Xie, X. Zhang *et al*., "Frequency-coupling admittance modeling of converter-based wind turbine generators and the control-hardware-in-the-loop validation," *IEEE Transactions on Energy Conversion*, vol. 35, no. 1, pp. 425-433, Mar. 2020.

[3] P. Mitra, L. Zhang, and L. Harnefors, "Offshore wind integration to a weak grid by VSC-HVDC links using power-synchronization control: a case study," *IEEE Transactions on Power Delivery*, vol. 29, no. 1, pp. 453-461, Feb. 2014.

[4] M. Liserre, R. Teodorescu, and F. Blaabjerg, "Stability of photovoltaic and wind turbine grid-connected inverters for a large set of grid impedance values," *IEEE Transactions on Power Electronics*, vol. 21, no. 1, pp. 263-272, Jan. 2006.

[5] L. Zhang, L. Harnefors, and H.-P. Nee, "Power-synchronization control of grid-connected voltage-source converters," *IEEE Transactions on Power Systems*, vol. 25, no. 2, pp. 809-820, May 2010.

[6] K. M. Alawasa and Y. A. I. Mohamed, "Impedance and damping characteristics of grid-connected VSCs with power synchronization control strategy," *IEEE Transactions on Power Systems*, vol. 30, no. 2, pp. 952-961, Mar. 2015.

[7] T. Knuppel, J. N. Nielsen, K. H. Jensen *et al*., "Small-signal stability of wind power system with full-load converter interfaced wind turbines," *IET Renewable Power Generation*, vol. 6, no. 2, pp. 79-91, Mar. 2012.

[8] J. Morató, T. Knüppel, and J. Østergaard, "Residue-based evaluation of the use of wind power plants with full converter wind turbines for power oscillation damping control," *IEEE Transactions on Sustainable Energy*, vol. 5, no. 1, pp. 82-89, Jan. 2014.

[9] J. Quintero, V. Vittal, G. T. Heydt *et al*., "The impact of increased penetration of converter control-based generators on power system modes of oscillation," *IEEE Transactions on Power Systems*, vol. 29, no. 5, pp. 2248-2256, Sept. 2014.

[10] J. Ma, Y. Qiu, Y. Li *et al*., "Research on the impact of DFIG virtual inertia control on power system small-signal stability considering the phase-locked loop," *IEEE Transactions on Power Systems*, vol. 32, no. 3, pp. 2094-2105, May 2017.

[11] W. Du, X. Chen, and H. Wang, "Power system electromechanical oscillation modes as affected by dynamic interactions from grid-connected PMSGs for wind power generation," *IEEE Transactions on Sustainable Energy*, vol. 8, no. 3, pp. 1301-1312, Jul. 2017.

[12] W. Du, X. Chen, and H. Wang, "PLL-induced modal resonance of grid-connected PMSGs with the power system electromechanical oscillation modes," *IEEE Transactions on Sustainable Energy*, vol. 8, no. 4, pp. 1581-1591, Oct. 2017.

[13] H. Liu, X. Xie, J. He *et al*., "Subsynchronous interaction between direct-drive PMSG based wind farms and weak AC networks," *IEEE Transactions on Power Systems*, vol. 32, no. 6, pp. 4708-4720, Nov. 2017.

[14] C. Guo, J. Zhang, S. Yang *et al*., "A modified dynamic model and small-signal stability analysis for LCC-HVDC system," *CSEE Journal of Power and Energy Systems*, doi:10.17775/CSEEJPES.2021.05820

[15] W. Du, Z. Zhen, and H. Wang, "The sub-synchronous oscillations caused by an LCC HVDC line in a power system under the condition of near strong modal resonance," *IEEE Transactions on Power Delivery*, vol. 34, no. 1, pp. 231-240, Feb. 2019.

[16] W. Du, Q. Fu, and H. Wang, "Strong dynamic interactions between multi-terminal DC network and AC power systems caused by open-loop modal coupling," *IET Generation, Transmission & Distribution*, vol. 11, no. 9, pp. 2362-2374, Jun. 2017.

[17] W. Du, Q. Fu, and H. Wang, "Sub-synchronous oscillations caused by open-loop modal coupling between VSC-based HVDC line and power system," *IEEE Transactions on Power Systems*, vol. 33, no. 4, pp.

3664-3677, Jul. 2018.
[18] W. Du, Q. Fu, and H. Wang, "Method of open-loop modal analysis for examining the sub-synchronous interactions induced by the VSC control in an MTDC/AC power system," *IEEE Transactions on Power Delivery*, vol. 33, no. 2, pp. 840-850, Apr. 2018.
[19] J. G. Slootweg and W. L. Kling, "The impact of large scale wind power generation on power system oscillations," *Electric Power Systems Research*, vol. 67, no. 1, pp. 9-20, Oct. 2003.
[20] Y. C. Choo, A. P. Agalgaonkar, K. M. Muttaqi *et al*., "Analysis of subsynchronous torsional interaction of HVDC system integrated hydro units with small generator-to-turbine inertia ratios," *IEEE Transactions on Power Systems*, vol. 29, no. 3, pp. 1064-1076, May 2014.
[21] L. Fan, Z. Mao, and D. Osborn, "Wind farms with HVDC delivery in load frequency control," *IEEE Transactions on Power Systems*, vol. 24, no. 4, pp. 1894-1895, Nov. 2009.
[22] Z. Miao, L. Fan, D. Osborn *et al*., "Wind farms with HVDC delivery in inertial response and primary frequency control," *IEEE Transactions on Energy Conversation*, vol. 25, no. 4, pp. 1171-1178, Dec. 2010.
[23] M. Wang, Y. Chen, X. Dong *et al*., "Impedance modeling and stability analysis of DFIG wind farm with LCC-HVDC transmission," *IEEE Journal on Emerging and Selected Topics in Circuits Systems*, vol. 12, no. 1, pp. 7-19, Mar. 2022
[24] Z. Zhen, W. Du, and H. Wang, "The simulation study on SSOs caused by the HVDC under the condition of near strong modal resonance," *Proceedings of the CSEE*, vol. 39, no. 7, pp. 1976-1984, Apr. 2019.
[25] B. Gao, Y. Liu, Y. Li *et al*., "Analysis on disturbance transfer path and damping characteristics of sub-synchronous interaction between D-PMSG-based wind farm and LCC-HVDC," *Proceedings of the CSEE*, vol. 41, no. 5, pp. 1713-1728, Mar. 2021.
[26] S. G. Vennelaganti and N. R. Chaudhuri, "New insights into coupled frequency dynamics of AC grids in rectifier and inverter sides of LCC-HVDC interfacing DFIG-based wind farms," *IEEE Transactions on Power Delivery*, vol. 33, no. 4, pp. 1765-1776, Aug. 2018.
[27] M. Zhang, X. Yuan, and J. Hu, "Mechanism analysis of subsynchronous torsional interaction with PMSG-based WTs and LCC-HVDC," *IEEE Journal of Emerging and Selected in Topics Power Electronics*, vol. 9, no. 2, pp. 1708-1724, Apr. 2021.
[28] B. Gao, Y. Wang, S. Zeng *et al*., "Analysis of sub-synchronous component path and damping characteristics of D-PMSG-based wind farm incorporated into weak AC grid," *Proceedings of the CSEE*, vol. 42, no. 14, pp. 5089-5103, Jul. 2022.
[29] B. Gao, Y. Liu, and X. Wang, "Subsynchronous oscillation mechanism analysis of direct-drive wind farm with VSC-HVDC system based on path analysis method," *Proceedings of the CSEE*, doi:10.13334/j.0258-8013. pcsee.221589
[30] B. Gao, Y. Liu, R. Song *et al*., "Study on subsynchronous oscillation characteristics of DFIG-based wind farm integrated with LCC-HVDC system," *Proceedings of the CSEE*, vol. 40, no. 11, pp. 3477-3489, Jun. 2020.
[31] B. Gao, S. Chen, and Y. Liu, "Analysis on coupling path and damping characteristics of sub-synchronous oscillation between photovoltaic and LCC-HVDC system," *Automation of Electric Power Systems*, vol. 46, no. 24, pp. 66-75, Dec. 2022.
[32] Q. Geng, H. Sun, X. Zhou *et al*., "A storage-based fixed-time frequency synchronization method for improving transient stability and resilience of smart grid," *IEEE Transactions on Smart Grid*, doi:10.1109/TSG.2023. 3259685
[33] Q. Geng, H. Sun, X. Zhang *et al*., "Mitigation of oscillations in three phase LCL-filtered grid converters based on proportional resonance and improved model predictive control," *IEEE Transactions on Industry Applications*, vol. 59, no. 2, pp. 2590-2602, Mar.-Apr. 2023.
[34] F. Yu, X. Wang, Y. Yang *et al*., "An application of hybrid genetic algorithm in the parameters optimization of HVDC constant current controller," *Power System Protection and Control*, vol. 42, no. 9, pp. 126-131, May 2014.
[35] Y. Ye, J. Wang, W. Chen *et al*., "Controller parameters optimization method for LCC-HVDC system based on small-interference dynamic model," *Southern Power System Technology*, vol. 15, no. 4, pp. 1-9, Apr. 2021.
[36] A. Zheng, C. Guo, Z. Yin *et al*., "Optimal adjustment method of control parameters for improving small-signal stability of hybrid multi-terminal HVDC system under weak AC condition," *Transactions of China Electrotechnical Society*, vol. 35, no. 6, pp. 1336-1345, Mar. 2020.
[37] W. Liu, B. Qin, R. Zhang *et al*., "Optimal design method of control parameters for MMC-MTDC," *Electric Machines and Control*, vol. 25, no. 2, pp. 10-18, Feb. 2021.
[38] B. Shao, S. Zhao, Y. Yang *et al*., "Sub-synchronous oscillation characteristics and analysis of direct-drive wind farms with VSC-HVDC systems," *IEEE Transactions on Sustainable Energy*, vol. 12, no. 2, pp. 1127-1140, Apr. 2021.
[39] C. Guo, Z. Yin, Y. Wang *et al*., "Investigation on small-signal stability of hybrid LCC-MMC HVDC system," *Proceedings of the CSEE*, vol. 39, no. 4, pp. 1040-1052, Apr. 2019.

Liwen Zheng received the B.S. degree from Yanshan University, Qinhuangdao, China, in 2018, the M.S. degree in electrical engineering from North China Electric Power University, Baoding, China, in 2021. She is currently pursuing the Ph.D. degree in the Power System Department at China Electric Power Research Institute, Beijing, China. Her research interests include power system stability and control.

Shiying Ma received the B.S. degree from Xi'an Jiaotong University, Xi'an, China, and the M.S. and Ph.D. degrees in electrical engineering from China Electric Power Research Institute, Beijing, China. He is currently the Deputy Director of Power System Department. His research interests include power system dynamics, stability and control.